Journal of Molecular Modeling (2022) 28: 160
https://doi.org/10.1007/s00894-022-05136-5

ORIGINAL PAPER

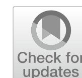

The loading speed facilitating stress relaxation behaviors of surface-modified silicon: a molecular dynamics study

Juan Chen[1] · Liang Fang[2,3] · Huiqin Chen[1] · Kun Sun[3] · Shu'e Dang[1] · Jing Han[4]

Received: 29 July 2021 / Accepted: 30 April 2022 / Published online: 21 May 2022
© The Author(s), under exclusive licence to Springer-Verlag GmbH Germany, part of Springer Nature 2022

Abstract
Time-dependent plastic deformation commonly exists in silicon-based microelectronic contact. The stress relaxation behaviors of SiO_2/Si bilayer composite are studied using molecular dynamics simulation by varying loading speed. The results imply that the indentation force decreases sharply at the initial and linearly towards the end of holding, and the amount of stress relaxation increases with the increasing loading speed. The plastic deformation of confined amorphous SiO_2 film is carefully analyzed based on the amorphous plasticity theories; variations of coordinated silicon atoms and Si–O bond number indicate that the films are further densified at different degrees depending upon loading speed during holding. The densification is strengthened at a higher speed because much more activated shear transformation zones (STZs) and accumulated free volume generate within films indented at higher speed. The phase transformation of monocrystalline silicon is observed in indented silicon during holding; the Si-II and bct-5 silicon atoms increase with time and loading speed.

Keywords Stress relaxation behaviors · SiO_2/Si bilayer composite · Loading speed · Plastic deformation · Molecular dynamics simulation

Introduction

Monocrystalline silicon, as one of the most popular semiconductor materials, is widely used in the manufacture of micro-electro-mechanical systems (MEMS), precision optics elements, and electronic products [1]. An amorphous SiO_2 film served as a dielectric layer and mechanical component locates on the top surface of monocrystalline silicon [2], affecting the time-dependent mechanical properties (creep or stress relaxation) of Si-based devices [3]. The stress exponent n at steady-state creep can reveal the mechanisms of the time-dependent plastic deformation. An interface diffusion mechanism dominates the creep deformation at shallow indentation depth region for amorphous materials, while the intrinsic creep behaviors for Zr-based metallic glasses (MGs) at deep depth region were observed [4]. This deformation mechanism was depicted by the "STZs" and "free volume" models based on the amorphous plasticity theories [5–7]. The STZs are small clusters of randomly close-packed atoms that spontaneously and cooperatively reorganize as applied shear stress exceeds its yield stress [8]. The operation of STZs creates a localized distortion of the surrounding materials and triggers the autocatalytic formation of shear bands, resulting in the accumulation of free volume during the localized shearing process. This deformation mechanism is different from what takes place within crystalline materials, i.e., grain boundary diffusion [9], grain sliding [10], and the dislocation governed plasticity [11].

Instantaneous plastic deformation at the onset of holding affects subsequent creep flow [12–14]. At higher load and/or faster loading, much more activated STZs and accumulated free volume are thought to be generated, leading to better atomic mobility, homogeneous deformation in MG [15], and

✉ Huiqin Chen
chenhuiqin@tyust.edu.cn

✉ Shu'e Dang
shuedang@163.com

[1] School of Materials Science and Engineering, Taiyuan University of Science and Technology, Taiyuan 030024, China

[2] School of Mechanical & Electrical Engineering, Xiamen University Tan Kah Kee College, Zhangzhou 363105, China

[3] State Key Laboratory for Mechanical Behavior of Materials, Xi'an Jiaotong University, Xi'an 710049, China

[4] School of Mechanical and Electrical Engineering, China University of Mining and Technology, Xuzhou 221116, China

lower stress exponent n [4]. The mechanism of nanoindentation creep for plasma-enhanced chemical vapor deposited silicon oxide thin film (SiO_x) was investigated and reported that as-deposited state exhibited a strong indentation size effect of n [16], which was much reduced after rapid thermal annealing [17]. For monocrystalline silicon, the dislocation glide is the primary creep mechanism at elevated temperatures (from 800 to 1300 °C) and low stress (from 2 to 150 MPa) through uniaxial compression and bending tests [18]. Creep testing of fully lithiated silicon nanowires was performed at fixed force levels above and below the yield stress, reporting that the creep mechanism transformed from diffusional to dislocation-mediated in nature [19]. Electron-beam irradiation greatly enhanced creep deformation of amorphous silicon nano-cantilever and resulted in the reduction of n [20]. The size effects of silicon micro-samples were studied; the creep results of silicon diaphragms annealed at 900 °C under atmospheric pressure showed that large diaphragms have a higher risk of creep. No creep effects were visible when the diaphragm radius is below a certain value [21]. The creep rate of silicon cantilever microbeams increases at the temperature of 600 ~ 700 °C and under the stress of 235 ~ 501 MPa, and the duration of the steady-state creep decreases with the increasing temperature or stress [22]. The phase transformation coupled with the dislocation activities however dominates the deformation mechanism under nanoindentation at room temperature [23–25]. Though much efforts have been paid to amorphous materials and crystalline silicon, the specific time-dependent features of confined film and bilayer composites during nanoindentation process, especially at atomic scale, are still unclear because of limitation of experimental conditions.

In this study, the stress relaxation behaviors of monocrystalline silicon covered with an amorphous SiO_2 film are studied through nanoindentation using molecular dynamics (MD) simulation by varying the loading speed. Focuses are put on the time-dependent behaviors of SiO_2/Si bilayer composite and plastic deformation characteristics of both amorphous SiO_2 film and monocrystalline silicon. This study may contribute to a better understanding of stress relaxation of confined amorphous SiO_2 film and guide MEMS design.

Modeling and methods

In this work, the simulations are conducted using LAMMPS open-source software [26]. The nanoindentation system of stress relaxation for SiO_2/Si bilayer composite is composed of a spherical diamond indenter and a monocrystalline silicon covered with an amorphous SiO_2 film (SiO_2/Si bilayer composite). The radius of spherical indenter is 6 nm. The silicon substrate has a size of $30 \times 30 \times 25$ nm^3; it contains 1,130,685 atoms. Its crystallographic orientation is [100], [010], and [001] along X, Y, and Z axes, respectively. The amorphous SiO_2 film, with a size of $30 \times 30 \times 1$ nm^3, is set on the top surface of silicon. The film is prepared by quenching melted beta-cristobalite similar to the work of Chowdhury [27]. In this work, the atoms within the bilayer composite are divided into three areas, the frozen area, the thermostatic area, and the newton area. The frozen area locates at the bottom to stabilize the sample. The thermostatic area adjacent to the frozen area is set to maintain a constant temperature during the whole nanoindentation. The thickness of the frozen and thermostatic areas is 1.0 and 1.5 nm, respectively. The remaining are newton atoms, which can integrate according to Newton's second law; the illustration refers to ref. [34]. The periodic boundary conditions are imposed in X and Y axes, while non-periodic boundary conditions are applied in Z axis.

To depict the interatomic relations between Si–Si, O–O, and Si–O atoms within the bilayer substrate, the extended Tersoff potential based on ab initio calculations by Munetoh [28] was employed. This potential has been successfully adopted to describe interactions of amorphous SiO_2 [29, 30]. The interactions between Si atoms and C atoms of diamond indenter are described by the widely used Morse potential [31], the atomic potential energy expressed as:

$$E = \sum_{ij} D_0 \left[e^{-2\alpha(r-r_0)} - 2e^{-\alpha(r-r_0)} \right] \tag{1}$$

where $D_0 = 0.435$ eV, $\alpha = 4.6487$ Å^{-1}, $r_0 = 1.9475$ Å, and r represent cohesive energy, elastic modulus, interatomic equilibrium distance, and instantaneous distance, respectively. Lennard–Jones potential with the parameters $\varepsilon = 0.1$ eV and $\sigma = 3.275$ Å is utilized to describe the interactions of C–O atoms.

The interactions of C–C atoms are neglected due to its rigid body characteristic.

The process of stress relaxation simulation through nanoindentation involves three periods: relaxation, loading, and holding. To stabilize the simulation system, relaxation is conducted using NVT ensemble at 300 K for 90 ps. The nanoindentation loading is performed along the –Z direction by controlling the displacement of the indenter at a constant rate of 25 ms^{-1} until the indentation depth reaches 5.6 nm. Then the indenter remains unchanged for 200 ps during holding, as shown in Fig. 1. During the whole indentation process, the NVE ensemble with Langevin thermostat is adopted to control the simulation of 300 K, and the motion of Newtonian atoms is integrated with a velocity-Verlet algorithm with a time step of 0.5 fs.

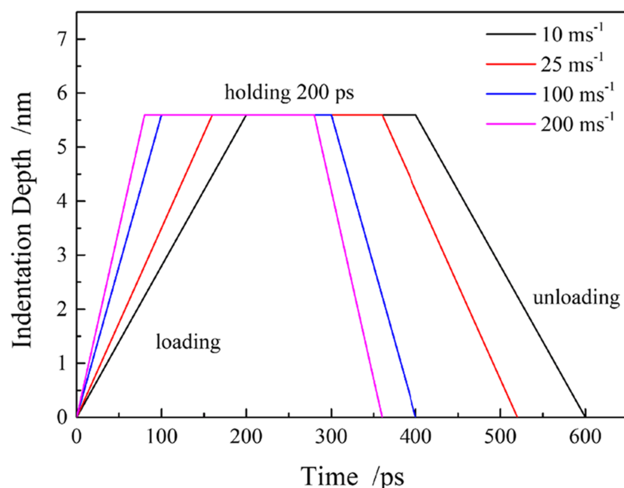

Fig. 1 Schematic of MD simulation for nanoindentation stress relaxation

Results and discussions

Stress relaxation features of SiO_2/Si bilayer composite

The time-dependent stress relaxation behaviors of SiO_2/Si bilayer composite are performed through nanoindentation with a spherical diamond indenter. The indenter penetrates the bilayer sample at various speeds (10, 25, 100, and 200 ms^{-1}) separately until the indentation depth grows to 5.6 nm, then the indenter remains unchanged for 200 ps. The indentation force during holding is monitored, as shown in Fig. 2. The indentation force declines dramatically at the beginning and almost linearly towards the end of holding. It is also found that the reduced rate of indentation force at the initial of holding increases with increasing loading speed; it reverses however as the holding time is larger than 50 ps. The decreased indentation force during holding is calculated in Fig. 2b, showing the higher loading speed enhances the stress relaxation of tested samples, which is consistent with Wang and Huang's results [4, 32].

It is worth noting from Fig. 2a that the indentation force at the initial of holding differs at various loading speeds, which results from the response of SiO_2/Si bilayer composite to different loading speeds. The indentation force variations as a function of indentation depth at different speeds are illustrated in Fig. 3; the curves of indentation force and depth almost overlap with each other and a slight increase appears in indentation force at higher speed from 0.0 to 5.0 nm, then the indentation force drops at different degrees depending upon various loading speeds (100 ms^{-1} and 200 ms^{-1}). The higher the loading speed, the more indentation force declines. This is because the higher speed leads to the appearance of higher strain energy and activated STZs within amorphous SiO_2 films. The operation of activated STZs generates the free volume, and the accumulated free volume in turn favors the operation of STZs, resulting in an increasing number of defects and a decrease in mechanical stiffness of bilayer composite at higher loading speed [33].

Plastic deformation of SiO_2 film

To deeply understand the plastic deformation of amorphous SiO_2 film, its deformation features during the loading period

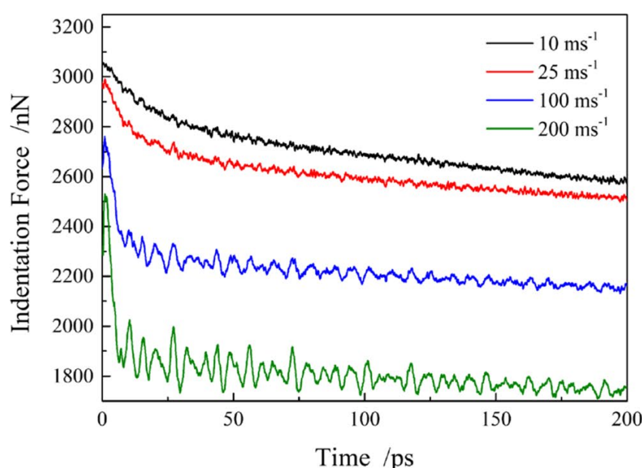

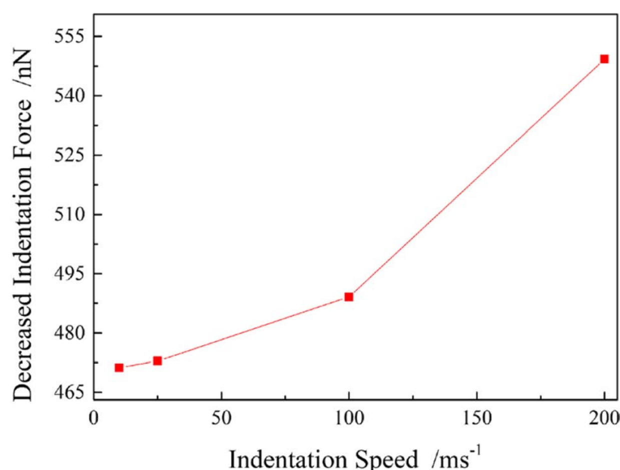

Fig. 2 Changes of indentation force for SiO_2/Si samples indented at different speeds. **a** Variations of indentation force versus time. **b** Changings of indentation force versus speed

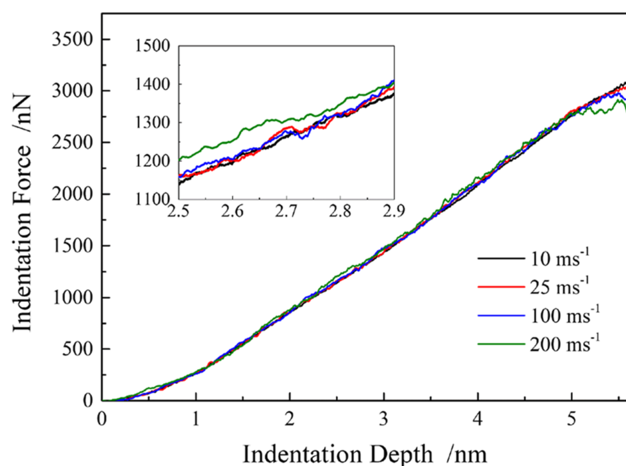

Fig. 3 The relationships between force and indentation depth during loading

are first probed and the number of coordinated-x silicon atoms (NCNx) of SiO_2 film is therefore employed. The variations of NCNx and Si–O bond as a function of indentation depth are illustrated in Fig. 4; it is observed that the NCN2 and NCN3 silicon atoms decrease as indentation depth varies from 0.0 to 4.2 nm, then increase sharply. The corresponding values of NCN2 and NCN3 are higher at a higher speed than those at a lower speed at the same indentation depth. The NCN4 decreases monotonously during the whole loading period with a lower decrease rate at shallow indentation and a higher decrease rate as the indentation depth exceeds 4.2 nm. Furthermore, the decrease rate increases with increasing loading speed. The NCN5 grows steadily and its values are lower at 200 ms^{-1} at the same indentation depth. The number variation of Si–O bond, which is a net result of the formation of Si–O bond due to densification and breakage owing to thinning, is analyzed within a cutoff of 0.2 nm during indentation in Fig. 4d. It shows that the

Fig. 4 Number variations of coordinated silicon atom and Si–O bond within SiO_2 film during loading. **a** NCN2. **b** NCN3. **c** NCN4 and NCN5. **d** number of Si–O bonds

number of Si–O bonds increases with growing indentation depth until the depth is more than 4.2 nm, then it declines dramatically. The corresponding values are much higher at a lower speed than those at higher speed at the same indentation depth, implying the amorphous SiO_2 film experiences a larger degree of densification at lower loading speed, while the film at higher speed exhibits less densification and tends to fracture preferentially. The reason for this is that much more STZs are activated and the resultant accumulated free volume within indented SiO_2 film favors the further deformation. On the other hand, there is not enough time for generated free volume to annihilate at a higher speed, increasing in accumulated free volume.

The partial atomic configuration of the film after loading is shown in Fig. 5; it is observed that the films are thinned to almost a single atomic layer and some small cavities exist within the films. The cavities within the film at 200 ms^{-1} are significantly larger, compared with those at 10 ms^{-1}, demonstrating the film at higher speed experiences larger plastic deformation and tends to fracture preferentially.

The plastic deformation of the indented films during holding are also studied in Fig. 6; the NCN2 atoms oscillate around zero at lower speeds (10 ms^{-1} and 25 ms^{-1}), while the number at higher speed (100 ms^{-1} and 200 ms^{-1}) declines sharply and then slowly as the relaxation time exceeds 50 ps. The increased NCN3 atoms decreases at lower speed and its values are slightly less at higher speed at the same time, except that at 200 ms^{-1}, where the NCN3 atoms increase and saturate around 40. The NCN4 decreases while NCN5 increases at a high rate as the time varies from 0 to 50 ps, then the NCN4 and NCN5 saturate at certain values. The absolute values of decreased NCN4 and increased NCN5 are significantly enhanced at a higher speed than those at a lower speed. The number variations of Si–O bonds during holding are also analyzed in Fig. 6d, showing that the values of Si–O bonds increase quickly at the initial and then steadily towards the end of holding. Its values grow with the increasing load speed, except those at 200 ms^{-1}, where the values are slightly less than those at 100 ms^{-1}. The decrease in NCN2, NCN3, and NCN4 atoms and increase in NCN5 atoms and Si–O bond number imply that the indented films are further densification during holding according to our previous work [34–36]. The degree of densification is strengthened with the increasing loading speed, except that at 200 ms^{-1}. This is contributed from the plastic deformation behaviors after loading; the higher loading speed promotes much more activated STZs and accumulated free volume within films, which favors the further deformation during the subsequent stress relaxation period. For the film at 200 ms^{-1}, further densification coupled with some elastic recovery occurs during holding.

Plastic deformation of monocrystalline silicon

The phase deformation occurs to monocrystalline silicon within the high-stressed regions as the film is indented. This follows the experimental researches and theory analysis that phase deformation dominates plasticity under point-contact conditions at room temperature. That is to say the original diamond cubic silicon (with 4-coordinated number) in silicon substrate transforms to metallic bct-5 (body-centered-tetragon, with 5-coordinated number) and Si-II (body-centered-tetragonal β-tin, with 6-coordinated number) phases in the nanoindentation [37–40]. Its deformation characteristics at different loading speeds are studied according to the coordinate number, as shown in Fig. 7. It is observed that the phase transformation atoms increase significantly with the growing indentation depth, and the curves of bct-5 phase atoms at different speeds almost overlap with each other, as well as the curves of Si-II phase atoms. In addition, the number of bct-5 silicon atoms is much higher than that of Si-II silicon at the same indentation depth; the phase distribution of Si(110) is shown in Fig. 8. It is found that the bct-5 and Si-II phase atoms at 10 ms^{-1} are much more than those at 200 ms^{-1}, where more disordered silicon atoms appear under deformed surface of silicon substrate. This implies that the much higher loading speed promote amorphization.

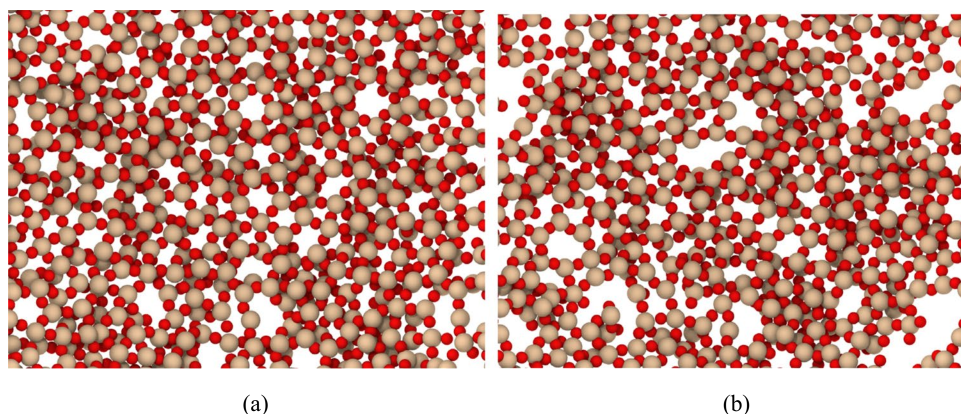

Fig. 5 The atomic configuration of indented SiO_2 after loading at different speeds. **a** SiO_2 film at 10 ms^{-1}. **b** SiO_2 film at 200 ms^{-1}

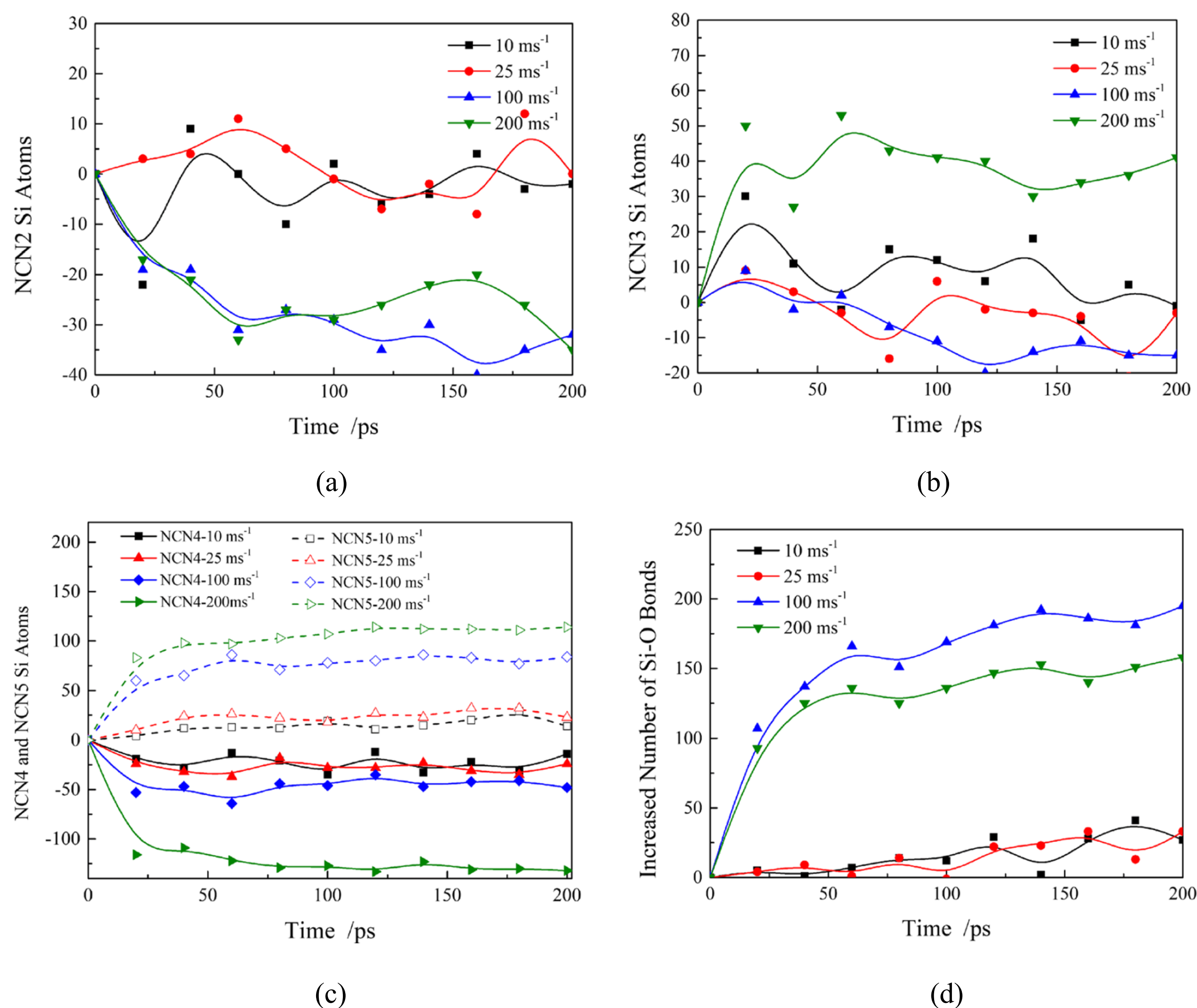

Fig. 6 Number variations of coordinated silicon atom and Si–O bond within SiO_2 film during holding. **a** NCN2. **b** NCN3. **c** NCN4 and NCN5. **d** number of Si–O bonds

Subsequently, the phase deformation of indented monocrystalline silicon during holding is analyzed in Fig. 9. It shows that the number of bct-5 silicon atoms raises sharply at the initial of holding, then it saturates as the time is larger than 50 ps. The values of generated bct-5 silicon atoms are much higher at higher speeds; e.g., they are 6000 and 1400 at 200 ms^{-1} and 10 ms^{-1} at the end of holding, respectively. The variations of Si-II atoms are somewhat similar to those of bct-5 atoms except those at 200 ms^{-1}. The corresponding values increase and then decline with the increasing loading speed during the same time, as shown in Fig. 9b. The values of Si-II atoms at 200 ms^{-1} are almost unchanged during holding. The differences in phase deformation atoms originate from the nature of monocrystalline silicon and the effects of loading speed.

The atomic configuration of phase deformation distribution for monocrystalline silicon substrate after holding is shown in Fig. 10, finding that the Si-II phase atoms, which are surrounded by numerous bct-5 phase atoms, locate at the middle of the indent. The amorphous silicon atoms are beneath the indented top surface. It is also observed that the Si-II silicon atoms decrease while the bct-5 silicon atoms increase with the loading speed after holding. These results imply that the Si-II and bct-5 silicon trend to amorphization during time-dependent stress relaxation after loaded at higher speed (200 ms^{-1}), where the applied shear stress is much higher compared with that at lower speed. Its values (30 GPa) exceed the transform stress from crystalline silicon to amorphous silicon (24 GPa) according to previous research [36, 41, 42]. This

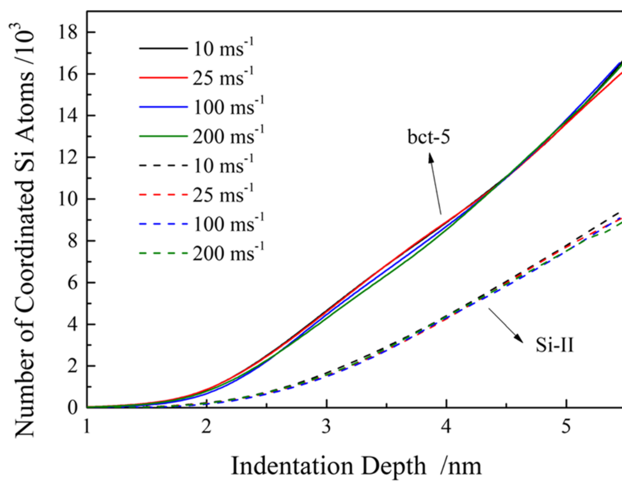

Fig. 7 Number variations of bct-5 and Si-II phase silicon atoms during loading

explains the number variations of bct-5 and Si-II phase atoms during holing.

Conclusions

The effects of loading speed on the stress relaxation behaviors of SiO_2/Si bilayer composite are conducted using molecular dynamics simulation; the results are concluded as follows:

(1) The indentation force decreases sharply at the initial and steadily towards the end of holding and the decreased indentation force increases with the increasing loading speed.
(2) The amorphous SiO_2 films are further densified during holding after loading at different speeds, and its degree of densification is enhanced at higher speed because much more activated STZs and accumulated free volume appear within films indented with higher speed.

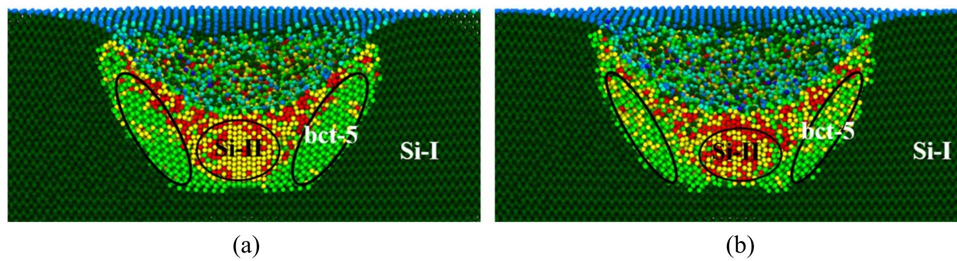

Fig. 8 The atomic configuration monocrystalline silicon after loading at different speeds. Silicon atoms are colored according the coordinate number. The dark green, light green, yellow, blue, and red atoms are Si-I, bct-5, Si-II, surface atoms, and other phase atoms, respectively. **a** Cross-section of Si (110) at 10 ms^{-1}. **b** Cross-section of Si(110) at 200 ms^{-1}

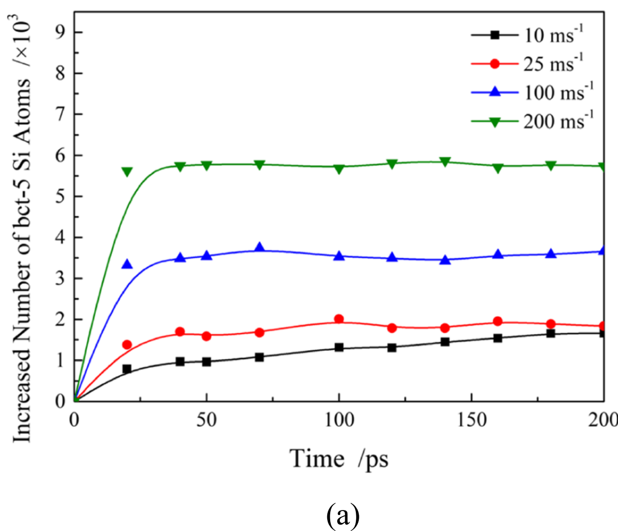

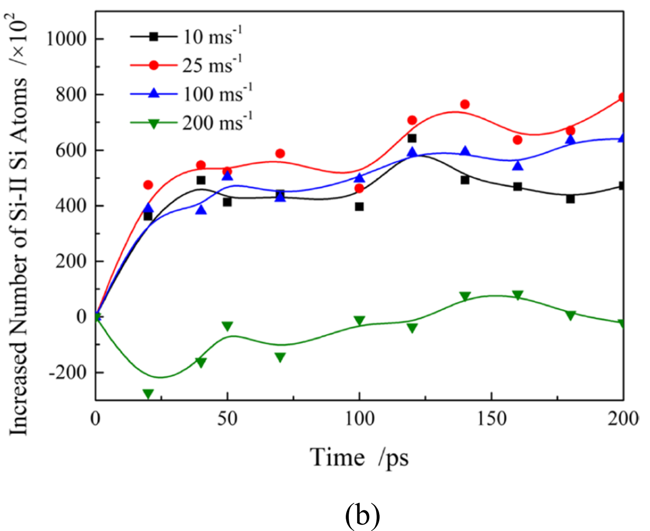

Fig. 9 Phase transformation of monocrystalline silicon during holding. **a** Number of bct-5 atoms. **b** Number of Si-II atoms

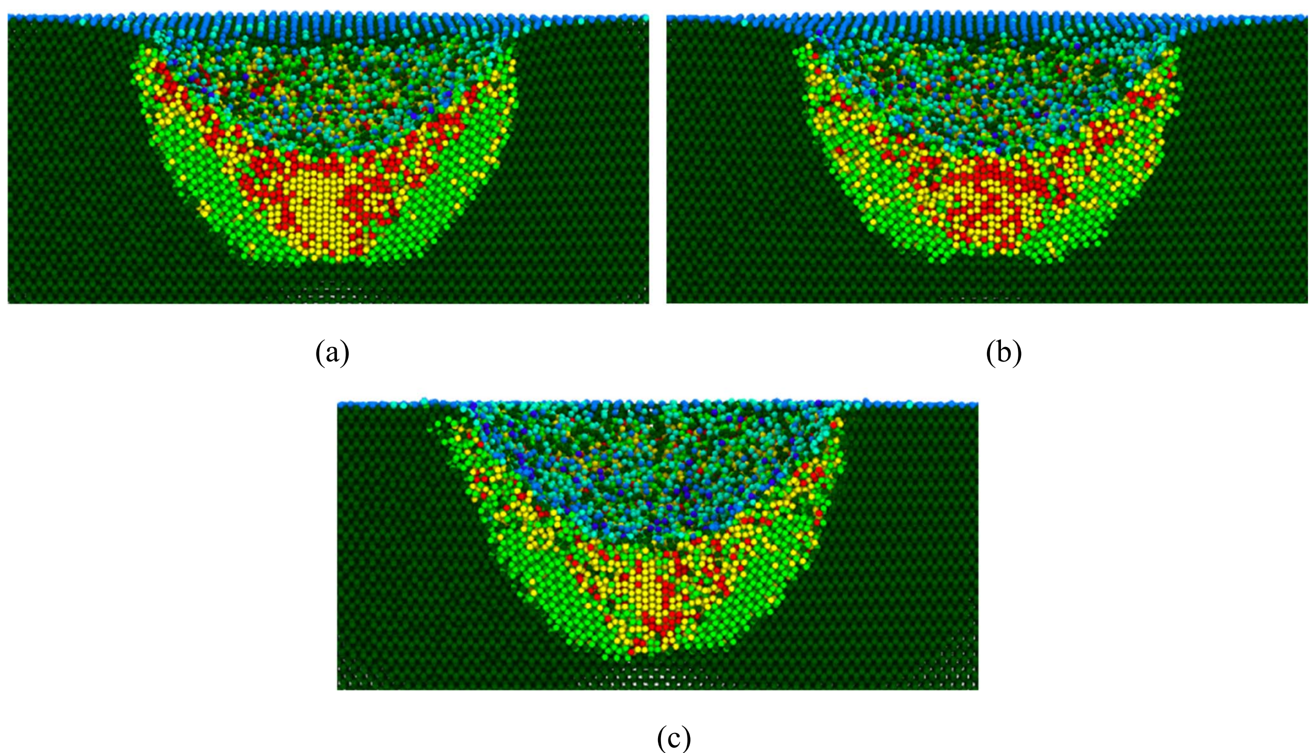

Fig. 10 The slice-section of the atomic configuration of phase deformation distribution of Si (110) after holding. The dark green, light green, yellow, blue, and red atoms are Si-I, bct-5, Si-II, surface atoms, and other phase atoms, respectively. **a** 10 ms^{-1}. **b** 100 ms^{-1}. **c** 200 ms^{-1}

(3) The phase transformation of monocrystalline silicon occurs during the stress relaxation period, i.e., the Si-II and bct-5 silicon atoms increase with relaxation time and loading speed.

Author contribution Juan Chen: investigation; formal analysis; writing—original draft; funding acquisition. Liang Fang: methodology, funding acquisition. Huiqin Chen: writing—review and editing; funding acquisition. Kun Sun: supervision. Shu'e Dang: writing—review and editing. Jing Han: conceptualization.

Funding This study is supported by the National Natural Science Foundation of China (51375364, 51575372) by Liang Fang and Huiqin Chen, respectively, and the Doctor Funds of Taiyuan University of Science and Technology (20202004) by Juan Chen.

Data availability Not applicable.

Code availability Not applicable.

Declarations

Competing interests The authors declare no competing interests.

References

1. Du X, Zhao H, Zhang L, Yang Y, Xu H, Fu H, Li L (2015) Molecular dynamics investigations of mechanical behaviours in monocrystalline silicon due to nanoindentation at cryogenic temperatures and room temperature, Sci Rep, 5.
2. Blasco X, Hill D, Porti M, Nafria M, Aymerich X (2001) Topographic characterization of AFM-grown SiO_2 on si. Nanotechnology 12:110–112
3. Cao ZQ, Zhang X (2004) Density change and viscous flow during structural relaxation of plasma-enhanced chemical-vapor-deposited silicon oxide films. J Appl Phys 96:4273–4280
4. Wang F, Li JM, Huang P, Wang WL, Lu TJ, Xu KW (2013) Nanoscale creep deformation in Zr-based metallic glass. Intermetallics 38:156–160
5. Spaepen F (2006) Homogeneous flow of metallic glasses: a free volume perspective. Scripta Mater 54:363–367
6. Spaepen F (1977) Microscopic mechanism for steady-state inhomogeneous flow in metallic glasses. Acta Metall 25:407–415
7. Argon AS (1979) Plastic-deformation in metallic glasses. Acta Metall 27:47–58
8. Schuh CA, Lund AC (2003) Atomistic basis for the plastic yield criterion of metallic glass. Nat Mater 2:449–452
9. Pal S, Meraj M (2016) Structural evaluation and deformation features of interface of joint between nano-crystalline Fe-Ni-Cr alloy and nano-crystalline Ni during creep process. Mater Des 108:168–182

10. Pal S, Meraj M (2019) Investigation of reorganization of a nanocrystalline grain boundary network during biaxial creep deformation of nanocrystalline Ni using molecular dynamics simulation, Journal of Molecular Modeling, 25.
11. Li H, Ngan AHW (2011) Size effects of nanoindentation creep. J Mater Res 19:513–522
12. Li F, Xie Y, Gu J, Song M, Ni S, Guo S, Liao X (2015) Inhomogeneous creep deformation in metallic glasses. Materials Science and Engineering a-Structural Materials Properties Microstructure and Processing 648:57–60
13. Chudoba T, Richter F (2001) Investigation of creep behaviour under load during indentation experiments and its influence on hardness and modulus results. Surf Coat Technol 148:191–198
14. Wang C, Cao QP, Wang XD, Zhang DX, Qu SX, Jiang JZ (2017) Time-dependent shear transformation zone in thin film metallic glasses revealed by nanoindentation creep. J Alloy Compd 696:239–245
15. Yoo B-G, Kim K-S, Oh J-H, Ramamurty U, Jang J-I (2010) Room temperature creep in amorphous alloys: influence of initial strain and free volume. Scripta Mater 63:1205–1208
16. Cao ZQ, Zhang X (2007) Nanoindentation creep of plasma-enhanced chemical vapor deposited silicon oxide thin films. Scripta Mater 56:249–252
17. Cao Z, Zhang X (2006) Size-dependent creep behaviour of plasma-enhanced chemical vapour deposited silicon oxide films. J Phys D Appl Phys 39:5054–5063
18. Taylor TA, Barrett CR (1972) Creep and recovery of silicon single-crystals. Mater Sci Eng 10:93
19. Boles ST, Thompson CV, Kraft O, Moenig R (2013) In situ tensile and creep testing of lithiated silicon nanowires, Appl Phys Lett, 103.
20. Hirakata H, Konishi K, Kondo T, Minoshima K (2019) Electron-beam enhanced creep deformation of amorphous silicon nano-cantilever, J Appl Phys, 126.
21. Juan R, Kinnell P, Geear M, Ward M, Craddock R (2010) The creep behaviour of the microfabricated silicon diaphragms at 900degC. Microelectron Eng 87:1213–1216
22. Liu H-K, Chao J-J (2015) Length effect on creep of silicon cantilever microbeams. Int J Damage Mech 24:947–964
23. Shikimaka O, Prisacaru A, Bruk L, Usatyi Y, Burlacu A (2012) Influence of loading holding time under quasistatic indentation on electrical properties and phase transformations of silicon. Surf Eng Appl Electrochem 48:444–449
24. Shikimaka O, Prisacaru A, Burlacu A (2015) Effect of long-term holding under contact loading on the specific features of phase changes in silicon. Mater Sci 51:405–411
25. Gerbig YB, Michaels CA, Cook RF (2016) In situ observations of Berkovich indentation induced phase transitions in crystalline silicon films. Scripta Mater 120:19–22
26. Plimpton S (1995) Fast parallel algorithms for short-range molecular-dynamics. J Comput Phys 117:1–19
27. Chowdhury SC, Haque BZ, Gillespie JW Jr (2016) Molecular dynamics simulations of the structure and mechanical properties of silica glass using ReaxFF. J Mater Sci 51:10139–10159
28. Munetoh S, Motooka T, Moriguchi K, Shintani A (2007) Interatomic potential for Si-O systems using Tersoff parameterization. Comput Mater Sci 39:334–339
29. Zhao S, Xue J (2015) Modification of graphene supported on SiO_2 substrate with swift heavy ions from atomistic simulation point. Carbon 93:169–179
30. Wang J, Rajendran AM, Dongare AM (2015) Atomic scale modeling of shock response of fused silica and alpha-quartz. J Mater Sci 50:8128–8141
31. Shi J, Chen J, Wei X, Fang L, Sun K, Sun J, Han J (2017) Influence of normal load on the three-body abrasion behaviour of monocrystalline silicon with ellipsoidal particle. RSC Adv 7:30929–30940
32. Huang P, Wang F, Xu M, Xu KW, Lu TJ (2010) Dependence of strain rate sensitivity upon deformed microstructures in nanocrystalline Cu. Acta Mater 58:5196–5205
33. Das CR, Dhara S, Jeng Y-R, Tsai P-C, Hsu HC, Raj B, Bhaduri AK, Albert SK, Tyagi AK, Chen LC, Chen KH (2010) Direct observation of amophization in load rate dependent nanoindentation studies of crystalline Si, Applied Physics Letters, 96.
34. Chen J, Shi JQ, Chen Z, Zhang M, Peng WX, Fang L, Sun K, Han J (2019) Mechanical properties and deformation behaviors of surface-modified silicon: a molecular dynamics study. J Mater Sci 54:3096–3110
35. Chen J, Shi J, Wang Y, Sun J, Han J, Sun K, Fang L (2018) Nanoindentation and deformation behaviors of silicon covered with amorphous SiO2: a molecular dynamics study. RSC Adv 8:12597–12607
36. Chen J, Shi J, Zhang M, Peng W, Fang L, Sun K, Han J (2018) Effect of indentation speed on deformation behaviors of surface modified silicon: a molecular dynamics study. Comput Mater Sci 155:1–10
37. Sun J, Xu B, Zhuo X, Han J, Yang Z, Jiang J, Ma A, Wu G, Chu PK (2020) Investigation of indenter-size-dependent nanoplasticity of silicon by molecular dynamics simulation. ACS Appl Electron Mater 2:3039–3047
38. Han J, Song Y, Tang W, Wang C, Fang L, Zhu H, Zhao J, Sun J (2019) Reveal the deformation mechanism of (110) silicon from cryogenic temperature to elevated temperature by molecular dynamics simulation, Nanomaterials, 9.
39. Sun J, Ma A, Jiang J, Han J, Han Y (2016) Orientation-dependent mechanical behavior and phase transformation of mono-crystalline silicon. J Appl Phys 119:095904
40. Sun J, Li C, Jing H, Ma A, Fang L (2017) Nanoindentation induced deformation and pop-in events in a silicon crystal: molecular dynamics simulation and experiment. Sci Rep 7:10282
41. Jang JI, Lance MJ, Wen SQ, Tsui TY, Pharr GM (2005) Indentation-induced phase transformations in silicon: influences of load, rate and indenter angle on the transformation behavior. Acta Mater 53:1759–1770
42. Han J, Xu S, Sun J, Fang L, Zhu H (2017) Pressure-induced amorphization in the nanoindentation of single crystalline silicon. RSC Adv 7:1357–1362

Publisher's note Springer Nature remains neutral with regard to jurisdictional claims in published maps and institutional affiliations.